Exp Fluids (2016) 57:83
DOI 10.1007/s00348-016-2163-3

RESEARCH ARTICLE

Estimation of the measurement uncertainty in magnetic resonance velocimetry based on statistical models

Martin Bruschewski[1] · Daniel Freudenhammer[2] · Waltraud B. Buchenberg[3] · Heinz-Peter Schiffer[1] · Sven Grundmann[4]

Received: 3 February 2016 / Revised: 5 April 2016 / Accepted: 7 April 2016 / Published online: 4 May 2016

Abstract Velocity measurements with magnetic resonance velocimetry offer outstanding possibilities for experimental fluid mechanics. The purpose of this study was to provide practical guidelines for the estimation of the measurement uncertainty in such experiments. Based on various test cases, it is shown that the uncertainty estimate can vary substantially depending on how the uncertainty is obtained. The conventional approach to estimate the uncertainty from the noise in the artifact-free background can lead to wrong results. A deviation of up to −75 % is observed with the presented experiments. In addition, a similarly high deviation is demonstrated with the data from other studies. As a more accurate approach, the uncertainty is estimated directly from the image region with the flow sample. Two possible estimation methods are presented.

1 Introduction

Magnetic resonance velocimetry (MRV) refers to all nuclear magnetic resonance imaging (MRI) techniques that allow a quantification of the flow field. In combination with rapid prototyping, flow models of arbitrary shape and complexity can be fabricated and the flow can be measured in an easy and cost-efficient way. This combination, enabling very short design cycle times, makes MRV a unique tool for experimental fluid mechanics. What has been lacking so far is a detailed discussion of the statistical models that are used to estimate the measurement uncertainty. This is the purpose of this study.

The scientific basis for flow measurements with MRI was established by Moran (1982). Since then, MRV has been widely used in medicine, for example to measure the velocities of the blood flow in the human vascular system (Pelc et al. 1994; Markl et al. 2012). Over the past decade, there has been a considerable amount of work addressing MRV in the field of engineering and science. Comprehensive reviews on the possibilities and constraints of MRV for fluid mechanics research are provided in Fukushima (1999), Elkins and Alley (2007), and Gladden and Sederman (2013). Recent examples of engineering studies employing MRV can be found in the field of turbo machinery (Benson et al. 2012; Coletti et al. 2013; Bruschewski et al. 2016), power generation (Lo et al. 2012; Piro et al. 2016), and gasoline engines (Freudenhammer et al. 2014), among other engineering disciplines (Onstad et al. 2011; Issakhanian et al. 2012; Grundmann et al. 2012a, b; Wassermann et al. 2013; Buchenberg et al. 2015).

As for any other measurement modality, it is essential to estimate the statistical uncertainty of the results. In MRV, the uncertainty of the velocity data is typically calculated from the standard deviation of the noise in the reconstructed image (Pelc et al. 1994). A prominent source of noise is the thermal noise from the MRI receiver chain (den Dekker and Sijbers 2014). In the absence of noise correlations, the entire image is homogeneously affected by this noise. Thus, it would be irrelevant in which part of the image the noise is measured. However, this assumption

✉ Martin Bruschewski
bruschewski@glr.tu-darmstadt.de

1 Institute of Gas Turbines and Aerospace Propulsion, Technische Universität Darmstadt, Darmstadt 64287, Germany

2 Institute of Fluid Mechanics and Aerodynamics, Center of Smart Interfaces, Technische Universität Darmstadt, Darmstadt 64287, Germany

3 Medical Physics, Department of Radiology, University Medical Center Freiburg, Freiburg 79106, Germany

4 Institute of Fluid Mechanics, University of Rostock, Rostock 18051, Germany

does not hold in actual images. Spurious signals, commonly termed imaging artifacts, can locally increase the noise. Especially in measurements of turbulent flows, random velocity changes between sampling instances can lead to motion artifacts that appear as signal 'ghosts' in the image. In case of Cartesian sampled k-space, the artifact formation extends across the entire image in the direction of the phase encoding.

The original guidelines for the uncertainty estimation in MRV do not address the issue of the inhomogeneous noise in the image (Pelc et al. 1994). Typically, the standard deviation of the noise is simply measured in an artifact-free background region. This approach is here defined as the 'conventional approach.' The artifact-free background is defined as the image part which is free of signal and (motion) artifacts. As a result, the conventional approach includes only the uncertainty associated with thermal noise, while the measured velocity data might be subject to higher uncertainty because of motion artifacts.

This issue is addressed here. Based on experiments with five test cases and measurement data from other studies, it is shown that the conventional approach can lead to a clear underestimation of the measurement uncertainty. Finally, it is demonstrated how the uncertainty estimate should be obtained instead. Two possible estimators are presented.

As a constraint, the scope of this study is limited to MRV velocity measurements in (statistically) stationary turbulent flows. Other MRV techniques such as turbulence measurements will not be considered here. Parallel imaging techniques with subsampled k-space such as GRAPPA (Griswold et al. 2002) and SENSE (Pruessmann et al. 1999) are also outside the scope of this paper. The main reason for this constraint is that the statistical noise model for these imaging techniques is still subject to current research (den Dekker and Sijbers 2014). All presented measurements are based on a conventional gradient echo sequence using a Cartesian sampled k-space.

2 Theory—statistical model

This section briefly describes the mathematics behind velocity measurements with MRV, which is necessary to understand the dependence between image noise and measurement uncertainty. Later in this section, the statistical models, relevant to this study, are presented.

2.1 Influence of noise on the reconstructed image

In general, the reconstructed magnetic resonance data set, termed image, is subject to noise. The complex image intensity $S(\mathbf{r})$ can be modeled as (den Dekker and Sijbers 2014):

$$S(\mathbf{r}) = Z(\mathbf{r}) + \mathcal{N}(\mathbf{r}) \tag{1}$$

with $\mathbf{r}$ as the generalized image coordinate. The parameter $Z(\mathbf{r})$ is the complex noise-free component of the image intensity and $\mathcal{N}(\mathbf{r})$ is the superimposed complex noise.

Modern MRI systems typically employ a large number of receiver coils to extend the coverage of the receiver system. A commonly used technique to combine the images from different coils is the sum-of-squares (SOS) technique (Roemer et al. 1990). Using this combination technique, the image magnitude $M(\mathbf{r})$, representing the spin density in the sample, is obtained as:

$$M(\mathbf{r}) = \sqrt{\sum_{k=1}^{L} {}^{k}S(\mathbf{r})\, {}^{k}S^{*}(\mathbf{r})} \tag{2}$$

where ${}^{k}S(\mathbf{r})$ represents the image from the kth coil and L is the total number of receiver coils. The asterisk * denotes complex conjugation. The noise-free component of the image magnitude is defined as:

$$A(\mathbf{r}) = \sqrt{\sum_{k=1}^{L} {}^{k}Z(\mathbf{r})\, {}^{k}Z^{*}(\mathbf{r})}. \tag{3}$$

In this context, the image phase $\Psi(\mathbf{r})$ is obtained as:

$$\Psi(\mathbf{r}) = \angle \sum_{k=1}^{L} {}^{k}S(\mathbf{r}) \tag{4}$$

where $\angle$ denotes the complex angle. The noise-free component of the image phase is defined as:

$$\Phi(\mathbf{r}) = \angle \sum_{k=1}^{L} {}^{k}Z(\mathbf{r}). \tag{5}$$

The SOS combination inherently includes a weighting of the individual images. Thus, images with weaker magnitude will contribute less to the final image magnitude and image phase. Note that this combination technique simplifies to a standard single coil acquisition if only one coil is used.

In velocity measurements, the image phase is made sensitive to the velocity in the sample. Typically, a phase difference, $\Delta\Psi(\mathbf{r})$, is measured to remove spurious phase effects. For the phase difference between two images, known as the two-point scheme, the SOS combination becomes (Bernstein et al. 1994):

$$\Delta\Psi(\mathbf{r}) = \angle \sum_{k=1}^{L} {}^{k,1}S(\mathbf{r})\, {}^{k,2}S^{*}(\mathbf{r}) \tag{6}$$

where ${}^{k,1}S(\mathbf{r})$ and ${}^{k,2}S(\mathbf{r})$ represent the two images obtained from the kth coil. Introducing the velocity sensitivity V_{enc}, the spatially dependent velocity information $u(\mathbf{r})$ is finally obtained as (Pelc et al. 1994):

$$u(\mathbf{r}) = \frac{V_{\text{enc}}}{\pi}\Delta\Psi(\mathbf{r}). \tag{7}$$

2.2 Statistical distribution of the image values

The noise in Eq. (1) is typically modeled as a complex additive white Gaussian noise (den Dekker and Sijbers 2014). Therefore, it is assumed that the real and imagery components of this noise have the same standard deviation. Furthermore, it is assumed that the standard deviation is identical for different receiver coils and that the noise is uncorrelated. This is usually ensured by a process which is known as decorrelation or noise prewhitening (Hansen and Kellman 2015).

Based on these assumptions, the statistical model relevant to this study is presented. In a SOS reconstruction with Eq. (2), the real and imaginary noise components are rectified. It can be shown that the distribution of the image magnitude follows a non-central χ distribution (Constantinides et al. 1997). The probability density function (PDF) for an individual data point in the image, termed voxel, is defined as:

$$p(M \mid \sigma_{\text{n}}, A, L) = \frac{A^{1-L}}{\sigma_{\text{n}}^2} M^L \exp\left(\frac{-(M^2+A^2)}{2\sigma_{\text{n}}^2}\right) I_{L-1}\left(\frac{MA}{\sigma_{\text{n}}^2}\right) \tag{8}$$

where σ_{n} is the standard deviation of the real and imaginary noise components and I_{L-1} is the $(L-1)$th modified Bessel function of first kind. Note that Eq. (8) simplifies to a central χ distribution for $A = 0$. Furthermore, for single coil acquisitions ($L = 1$), the distribution is equal to a Rician distribution. In the case that $A = 0$ and $L = 1$, the distribution is equal to a Rayleigh distribution.

The phase reconstruction in Eq. (4) is given by the nonlinear computation of the angle which makes it difficult to derive the exact PDF (Lathi 1998). However, it can be shown that the distribution of the image phase is asymptotically equal to a Gaussian distribution (Gudbjartsson and Patz 1995). The PDF for an individual voxel is approximated as:

$$p(\Psi \mid \Phi, \sigma_\Psi) \approx \frac{1}{\sigma_\Psi\sqrt{2\pi}} \exp\left(-\frac{(\Psi-\Phi)^2}{2\sigma_\Psi^2}\right) \tag{9}$$

where σ_Ψ is the standard deviation of the image phase due to noise. Note that the distribution is independent of the number of receiver coils. Furthermore, it can be shown that σ_Ψ is approximately equal to the reciprocal value of the signal-to-noise ratio (SNR $= A/\sigma_{\text{n}}$) (Gudbjartsson and Patz 1995). The bias of this approximation is less than 1 % for SNRs larger than 8. In image coordinates, the approximation reads:

Table 1 Influence of the measurement scheme on the standard deviation of the phase difference (Pelc et al. 1991)

Method	Encoding example	$c_\Delta = \sigma_{\Delta\Psi}/\sigma_\Psi$
Two-point	$\Delta\Psi = \angle\sum {}^1S\,{}^2S^*$	$\sqrt{2}$
Six-point	$\Delta\Psi_x = \angle\sum {}^1S\,{}^2S^*$	$\sqrt{2}$
	$\Delta\Psi_y = \angle\sum {}^3S\,{}^4S^*$	
	$\Delta\Psi_z = \angle\sum {}^5S\,{}^6S^*$	
Four-point referenced	$\Delta\Psi_x = \angle\sum {}^1S\,{}^4S^*$	$\sqrt{2}$
	$\Delta\Psi_y = \angle\sum {}^2S\,{}^4S^*$	
	$\Delta\Psi_z = \angle\sum {}^3S\,{}^4S^*$	
Four-point balanced	$\Delta\Psi_x = \angle\sum {}^1S\,{}^2S\,{}^3S^*\,{}^4S^*/2$	1
	$\Delta\Psi_y = \angle\sum {}^1S\,{}^2S^*\,{}^3S\,{}^4S^*/2$	
	$\Delta\Psi_z = \angle\sum {}^1S\,{}^2S^*\,{}^3S^*\,{}^4S/2$	

For readability, the equations are written in simplified form, compared to Eq. (6)

$$\sigma_\Psi(\mathbf{r}) \approx \frac{\sigma_{\text{n}}(\mathbf{r})}{A(\mathbf{r})}. \tag{10}$$

The statistical distribution of a phase difference, as in Eq. (6), is related to the distribution of the individual image phases. Assuming that the individual images have identical SNR, the spatially dependent standard deviation of the phase difference, $\sigma_{\Delta\Psi}(\mathbf{r})$, is defined as:

$$\sigma_{\Delta\Psi}(\mathbf{r}) = c_\Delta\,\sigma_\Psi(\mathbf{r}) \tag{11}$$

where the factor c_Δ depends on the computation method that is used to obtain the phase difference. For a phase difference between two independent images, and hence uncorrelated noise, the factor is determined as $c_\Delta = \sqrt{2}$. This applies to the encoding of the velocity in one direction [two-point scheme, as in Eq. (6)]. The factor can significantly change for other measurement schemes. The values of c_Δ for common measurement schemes is provided in Table 1.

3 Methods—uncertainty estimation

The measurement uncertainty $\sigma_{\text{u}}(\mathbf{r})$ is defined as the standard deviation of the measured velocity values. It must be emphasized that the uncertainty does not include systematic errors, such as spatial misregistration or velocity encoding errors. In MRV, there are two possible ways to estimate the uncertainty from the image (Pelc et al. 1994). The uncertainty is directly calculated from the standard deviation of the phase difference:

$$\sigma_{\text{u}}(\mathbf{r}) = \frac{V_{\text{enc}}}{\pi}\sigma_{\Delta\Psi}(\mathbf{r}) \tag{12}$$

or more commonly, the uncertainty is obtained from the dependency on the SNR, using Eqs. (10) and (11):

$$\sigma_u(\mathbf{r}) \approx c_\Delta \frac{V_{enc}}{\pi} \frac{\sigma_n(\mathbf{r})}{A(\mathbf{r})}. \tag{13}$$

Generally, the measurement uncertainty is spatially dependent. However, since a voxel-wise estimation is not always possible, the measurement uncertainty is typically expressed as a constant value which is valid for the entire image, hence $\sigma_u(\mathbf{r}) \approx \hat{\sigma}_u$. The circumflex is used to distinguish an estimate from the true value.

The research on the parameter estimation in MRI has led to a number of review articles (e.g., Sijbers et al. 2007; Aja-Fernández et al. 2009). A list of some estimators is provided in Table 2. The following paragraphs focus on the estimation methods that are most applicable for standard MRV velocity measurements. Two constraints are considered: First, the estimator is designed for single coil and SOS-reconstructed images. And secondly, no access to the raw data or imaging sequence is required. Thus, the estimator is applied to the reconstructed image.

Based on these constraints, four selected uncertainty estimators are presented. The first two methods resemble the conventional approach of estimating the uncertainty from the noise in the artifact-free background. The latter two methods focus on the uncertainty estimation directly from the image region with the flow sample. In this context, the image background is termed 'BG' and the image region with the flow sample is termed 'ROI' (region of interest). Finally, the reference method is presented which will be used in the results section to evaluate the presented estimators.

3.1 Conventional approach (CA)—segmented image background ($\hat{\sigma}_{u,CA1}$)

As a widely used approach, the standard deviation of the noise is estimated from the image magnitude in the artifact-free background. The estimate is obtained from the second central moment of the central χ distribution (Constantinides et al. 1997):

$$\hat{\sigma}_n = \sqrt{\frac{1}{2L}\langle M^2(\mathbf{r}_{BG})\rangle} \tag{14}$$

where $\langle \ldots \rangle$ defines the sample mean and $M(\mathbf{r}_{BG})$ is a vector containing the magnitude values of the voxels in the artifact-free background. This method is sensitive to segmentation errors. Typically, a manual segmentation is required to remove all voxels not associated with the artifact-free background.

The noise-free image magnitude, necessary for Eq. (13), is measured in the ROI. From the second central moment of the non-central χ distribution it follows (Constantinides et al. 1997):

$$\hat{A} = \sqrt{\langle M^2(\mathbf{r}_{ROI})\rangle - 2L\,\hat{\sigma}_n^2} \tag{15}$$

where $M(\mathbf{r}_{ROI})$ is a vector containing the magnitude values of the voxels in the manually segmented ROI. Using both

Table 2 List of noise and signal estimators

Method	Associated density	References
Estimators that require prior segmentation of the image magnitude ($M(\mathbf{r})$)		
$\hat{\sigma}_n = \sqrt{2/(4-\pi)\,\mathrm{Var}\{M(\mathbf{r})\}}$	Rayleigh	Henkelman (1985)
$\hat{\sigma}_n = \sqrt{2/\pi}\langle M(\mathbf{r})\rangle$	Rayleigh	Henkelman (1985)
$\hat{\sigma}_n = \sqrt{\langle M^2(\mathbf{r})\rangle/2L}$	Central χ	Constantinides et al. (1997)
$\hat{A} = \sqrt{\langle M^2(\mathbf{r})\rangle - 2L\,\hat{\sigma}_n^2}$	Non-central χ	Constantinides et al. (1997)
$\hat{\sigma}_n^2 = \mathrm{Var}\{M(\mathbf{r})\}/\xi(\Theta, L)$	Non-central χ	Koay and Basser (2006)
$\hat{\sigma}_n = \sqrt{\mathrm{Var}\{M(\mathbf{r})\}}$	Gaussian	Kaufman et al. (1989)
$\hat{\sigma}_n = \sqrt{\mathrm{Var}\{{}^1M(\mathbf{r}) - {}^2M(\mathbf{r})\}/2}$	Gaussian	NEMA (2014)
$\hat{A} = \langle M(\mathbf{r})\rangle$	Gaussian	Kaufman et al. (1989)
Estimators that (might) require prior segmentation of the histogram ($h(M)$)		
$\hat{\sigma}_n = \arg\min_{\sigma_n, K} \sum \left[h(M) - K\frac{2^{1-L}}{\Gamma(L)}\frac{M^{2L-1}}{\sigma_n^{2L}}\exp(-\frac{M^2}{2\sigma_n^2})\right]$	Central χ	Aja-Fernández et al. (2009)
$\hat{\sigma}_n = \mathrm{mode}\{M(\mathbf{r})\}/\sqrt{2L-1}$	Central χ	Aja-Fernández et al. (2009)
$\left[\hat{\sigma}_n(j), \hat{A}(j)\right] = \arg\max_{\sigma_n, A} \sum_{i=1}^{N} \ln\left(p\left({}^iM(j) \mid \ldots\right)\right)$	Depending on p	Sijbers and den Dekker (2004)
Estimators that do not require prior segmentation		
$\hat{\sigma}_n = \mathrm{mode}\{\hat{\sigma}_{n,1}, \ldots, \hat{\sigma}_{n,W}\}$	Depending on $\hat{\sigma}_{n,w}$	Aja-Fernández et al. (2008)
$\hat{\sigma}_n = \arg\max_{\hat{\sigma}_{n,w}} \{\hat{p}(\hat{\sigma}_{n,w})\}$	Depending on $\hat{\sigma}_{n,w}$	

estimates, the measurement uncertainty is calculated with Eq. (13):

$$\hat{\sigma}_{\mathrm{u,CA1}} = c_\Delta \frac{V_{\mathrm{enc}}}{\pi} \frac{\hat{\sigma}_{\mathrm{n}}}{\hat{A}}. \tag{16}$$

3.2 Conventional approach (CA)—segmented image histogram ($\hat{\sigma}_{\mathbf{u,CA2}}$)

Similar to the previous estimator, the image magnitude in the background is used. From the central χ distribution, the standard deviation of the noise is estimated by searching for the maximum of the histogram (Aja-Fernández et al. 2009). The estimator is defined as:

$$\hat{\sigma}_{\mathrm{n}} = \frac{\mathrm{mode}\{M(\mathbf{r}_{\mathrm{BG}})\}}{\sqrt{2L-1}} \tag{17}$$

where the mode operator provides the value that appears most often in the vector $M(\mathbf{r}_{\mathrm{BG}})$, hence the peak of the corresponding histogram. In contrast to the mean of the same vector, the mode is insensitive to outlying data. A certain percentage of outliers, hence voxels not associated with the artifact-free background, will not affect Eq. (17). For this reason, it is sufficient to segment the image by a global magnitude threshold. The image region BG is defined as the voxels with low magnitude values and the ROI is defined as the voxels with high magnitude values. The determination of the threshold value will be demonstrated in the results section. The estimate obtained from Eq. (17) is then used to calculate the measurement uncertainty with Eq. (13):

$$\hat{\sigma}_{\mathrm{u,CA2}} = c_\Delta \frac{V_{\mathrm{enc}}}{\pi} \frac{\hat{\sigma}_{\mathrm{n}}}{\hat{A}} \tag{18}$$

where $\hat{A}$ is obtained similar to Eq. (15), except that the ROI is defined by the magnitude threshold.

3.3 ROI-based uncertainty—local statistics approach ($\hat{\sigma}_{\mathbf{u,ROI1}}$)

The standard deviation of the noise is estimated from the image magnitude in the ROI. This process is considerably more complicated than the noise estimation from the artifact-free background. The noise-free component of the image magnitude is typically not constant across the ROI. As a result, the noise in the ROI is modulated with systematic variations. These variations have typically a low spatial frequency and can be filtered out. However, the outcome will strongly depend on the specific filter characteristics.

As a more robust approach, the method of local statistics by Aja-Fernández et al. (2008) is used. In the original paper, the use of local statistics is proposed as an alternative to the segmentation of the image. The non-segmented image is divided into small windows, for which each a local estimate is calculated. The global estimate is then obtained as the most frequent value of all local estimates. This method produces accurate results even if some of the windows contain systematic variations of the image magnitude.

This technique is adopted here. First, the image is divided into small quadratic (or cubic) windows. Similar to the previous estimator, a magnitude threshold is used to define the voxels that belong to the ROI and to the BG. The windows that contain less ROI voxels than BG voxels are discarded. Based on this selection, a local estimate is then calculated for each remaining window. Aja-Fernández et al. (2008) propose the mode operator to find the most frequent value of the local estimates. However, it must be emphasized that the mode operator is only useful with discrete or coarsely rounded data. Calculating the mode with the continuous data of the local estimates is unlikely to provide a good estimate. Therefore, it is a more appropriate approach to fit a PDF onto the distribution of the local estimates and search for the peak of the fitted function. Accordingly, the global estimate is defined as:

$$\hat{\sigma}_{\mathrm{n}} = \arg\max_{\hat{\sigma}_{\mathrm{n,w}}} \left\{\hat{p}(\hat{\sigma}_{\mathrm{n,w}})\right\} \tag{19}$$

where $\hat{p}(\hat{\sigma}_{\mathrm{n,w}})$ is the PDF fitted onto the distribution of the local estimates $\hat{\sigma}_{\mathrm{n,w}}$. A suitable fitting approach is the kernel density estimation (Scott 2012). The kernel density estimation belongs to the category of nonparametric methods. Thus, the fitting process does not require a specification of the type of the PDF, which is extremely useful since the type of the distribution of the local estimates is generally unknown. The estimate obtained from Eq. (19) is then used to calculate the measurement uncertainty with Eq. (13):

$$\hat{\sigma}_{\mathrm{u,ROI1}} = c_\Delta \frac{V_{\mathrm{enc}}}{\pi} \frac{\hat{\sigma}_{\mathrm{n}}}{\hat{A}} \tag{20}$$

where $\hat{A}$ is obtained similar to Eq. (15), except that the ROI is defined by the magnitude threshold.

There are several ways to calculate the local estimates. For example, the iterative optimization scheme by Koay and Basser (2006) is used in combination with the sample variance ($\mathrm{Var}\{M(\mathbf{r})\} = \langle M^2(\mathbf{r})\rangle - \langle M(\mathbf{r})\rangle^2$) :

$$\hat{\sigma}^2_{\mathrm{n,w}} = \frac{\mathrm{Var}\{M(\mathbf{r}_{\mathrm{w}})\}}{\xi(\Theta, L)} \tag{21}$$

where $M(\mathbf{r}_{\mathrm{w}})$ is a vector containing the magnitude values of the voxels in the wth window. The correction function $\xi(\Theta, L)$ is derived from the moments of the non-central χ distribution:

$$\xi(\Theta, L) = 2L + \Theta^2 - \left[\sqrt{2}\frac{\Gamma(L+\frac{1}{2})}{\Gamma(L)}\,{}_1F_1\left(-\frac{1}{2}, L, -\frac{\Theta^2}{2}\right)\right]^2 \tag{22}$$

where ${}_1\mathrm{F}_1$ is the confluent hypergeometric function and Γ is the gamma function. The problem is iteratively solved by the fixed-point formula:

$$\Theta = \sqrt{\xi(\Theta, L)\left[1 + \frac{\langle M(\mathbf{r}_w)\rangle^2}{\mathrm{Var}\{M(\mathbf{r}_w)\}}\right] - 2L} \tag{23}$$

which has a unique solution; however, the convergence can be slow for small SNRs. It should be noted that for large SNRs, $\xi(\Theta, L)$ is close to one. Hence, it is not always necessary to perform the correction in Eq. (21).

3.4 ROI-based uncertainty—dual acquisition approach ($\hat{\sigma}_{\mathbf{u},\mathbf{ROI2}}$)

The uncertainty is estimated from the standard deviation of the phase difference data in the ROI. The velocity is typically inhomogeneous across the ROI, and therefore, the variation of the noise-free phase difference can be significant. The filtering of the phase difference data to obtain the component due to noise is complicated since the systematic variations can have the same spatial frequency and amplitude as the statistical variations. Also the local statistics approach from the previous method will not lead to reliable results because of this reason.

An approach that is insensitive to systematic variations in the image is the dual acquisition method (NEMA 2014). The adoption of this method for the phase difference data is straightforward. Using two repeated acquisitions, termed 'image replicas,' a third image is obtained as the difference between the two image replicas. Assuming that the difference is only due to noise, the standard deviation can be simply estimated from the variance of the Gaussian distribution in Eq. (9). Based on Eq. (12), the uncertainty estimator becomes:

$$\hat{\sigma}_{u,ROI2} = \frac{V_{enc}}{\pi}\sqrt{\frac{\mathrm{Var}\left\{{}^1\Delta\Psi(\mathbf{r}_{ROI}) - {}^2\Delta\Psi(\mathbf{r}_{ROI})\right\}}{2}} \tag{24}$$

where ${}^1\Delta\Psi(\mathbf{r}_{ROI})$ and ${}^2\Delta\Psi(\mathbf{r}_{ROI})$ are vectors containing the phase different values of all voxels in the ROIs from the first and second image, respectively. The factor 2 arises from the subtraction of the two statistically independent images.

3.5 Reference method ($\hat{\sigma}_{\mathbf{u},\mathbf{REF}}$)

The presented estimators rely on a number of assumptions, for example that the noise is constant across the selected image region or that the statistical noise model is true. A method with much weaker assumptions is the multiple replica method (Reeder et al. 2005; Dietrich et al. 2007). With this method, the measurement uncertainty is calculated as the standard deviation of the results in repeated 'identical' acquisitions. The measurement uncertainty is obtained voxel-wise; thus, for the *j*th voxel, the multiple replica estimate becomes:

$$\hat{\sigma}_u(j) = \frac{V_{enc}}{\pi}\sqrt{\mathrm{Var}\left\{{}^1\Delta\Psi(j), \ldots, {}^N\Delta\Psi(j)\right\}} \tag{25}$$

where ${}^i\Delta\Psi(j)$ with $i = [1, \ldots, N]$ is the phase difference value in the *j*th voxel and the *i*th image replica. N is the total number of image replicas. The ROI average of this estimate is then used as the reference value to validate the uncertainty estimators from Sects. 3.1–3.4:

$$\hat{\sigma}_{u,REF} = \langle \hat{\sigma}_u(\mathbf{r}_{ROI})\rangle. \tag{26}$$

In a similar way, the multiple replica method is used to determine the standard deviation of the noise for each individual voxel. This provides the distribution of the noise across the image. However, the estimation is more complicated than in Eq. (25) due to the non-central χ distribution of the image magnitude. The maximum likelihood method is applied, as suggested for such problems by Sijbers and den Dekker (2004). This method selects the parameter values of a given PDF with the aim to maximize the probability that the observed data belong to the resulting distribution. Using the PDF of the non-central χ distribution in Eq. (8), the maximum likelihood estimate is defined as:

$$\left[\hat{\sigma}_n(j), \hat{A}(j)\right] = \arg\max_{\sigma_n, A}\sum_{i=1}^{N}\ln\left(p\left({}^iM(j) \mid \sigma_n, A, L\right)\right) \tag{27}$$

where ${}^iM(j)$ is the magnitude value in the *j*th voxel and the *i*th image replica.

4 Results—experimental validation

Experiments are carried out with five different test cases. The description of these test cases is provided in Fig. 1 and Table 3. Test case 1 represents a reference case with the purpose to demonstrate the noise characteristics with a perfectly stationary fluid sample. Test cases (2a), (2b), and (2c) provide three different axial flows with a turbulence intensity of about 6 %. The flow rate, and therefore the magnitude of the turbulent fluctuations, increases from test case (2a) to test case (2c). The purpose of this setup is to show how a gradually increased flow unsteadiness affects the estimation of the measurement uncertainty. Finally, test case 3 provides a strongly swirling turbulent flow as a more realistic test case. Such swirling motion is found in many natural and technical flows, for example in the combustion chambers of gas turbines. In addition, test case 3 is set up as a 3D acquisition with a relatively large number of receiver coils. The flow rate and temperature for all test cases with flow are controlled by a flow conditioning unit similar to the one described in Grundmann et al. (2012b). The Reynolds numbers of these test

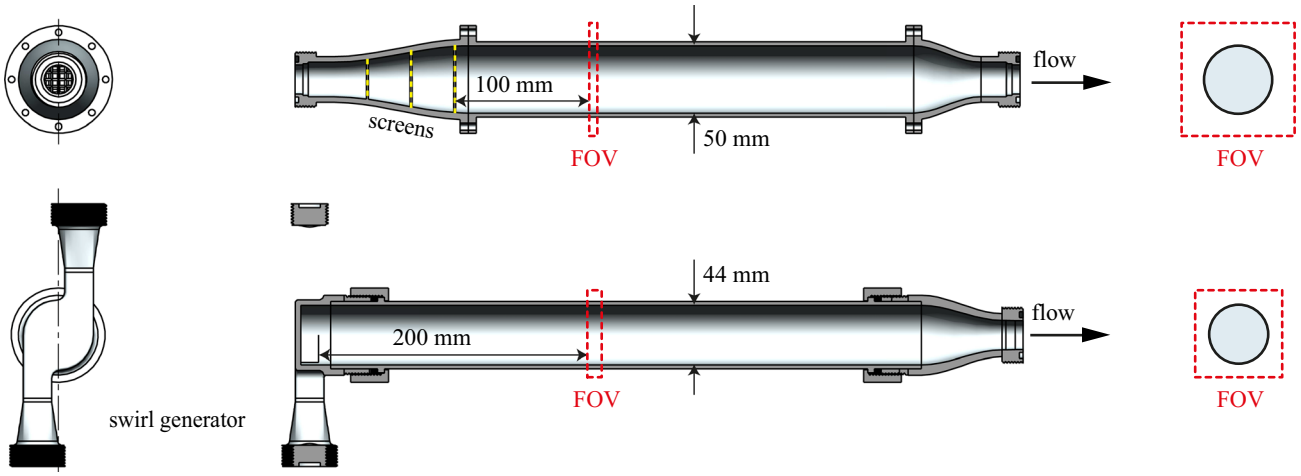

Fig. 1 Flow system for test case 2 (*top* drawings) and test case 3 (*bottom* drawings). The *left* drawings show the flow system perpendicular to the pipe axis, the *middle* drawings show the cut open view in the symmetry plane and the *right* drawings show the field of view (FOV) of the MRV acquisition perpendicular to the pipe axis

Table 3 Description of the measured test cases

1 (Reference): A cylindrical bottle is filled with a mixture of water, contrast agent, and hydroxyethylcellulose to prevent fluid motion. The 2D acquisition is conducted with a single receiver coil. Matrix size: $256 \times 256 \times 1$ ($0.6 \times 0.6 \times 2.8$ mm^3), echo time: $TE = 5.0$ ms, repetition time: $TR = 15.2$ ms, acquisition time: $TA = 3.9$ s, bandwidth: $BW = 605$ Hz/pixel	
2 (Axial Flow)	Water with contrast agent is pumped through a cylindrical pipe, as shown in Fig. 1 (top). The 2D acquisition is conducted with a single receiver coil. Matrix size: $128 \times 128 \times 1$ ($0.67 \times 0.67 \times 2.8$ mm^3), $TE = 5.0$ ms, $TR = 15.2$ ms, $TA = 2.0$ s, $BW = 605$ Hz/pixel
(a) $Re = 5000$, $U_b = 0.10$ m/s	
(b) $Re = 10{,}000$, $U_b = 0.20$ m/s	
(c) $Re = 15{,}000$, $U_b = 0.30$ m/s	
3 (Swirl Flow) $Re = 10{,}000$, $U_b = 0.23$ m/s: Water with contrast agent is pumped through a cylindrical pipe superimposed with a swirling motion, as shown in Fig. 1 (bottom). The 3D acquisition is conducted with $L = 12$ surface coils. Matrix size: $96 \times 96 \times 10$ ($1 \times 1 \times 1$ mm^3), $TE = 4.9$ ms, $TR = 15.8$ ms, $TA = 15.3$ s, $BW = 455$ Hz/pixel	

cases correspond to the bulk flow velocity U_b and the pipe diameter.

The MRV acquisitions are performed on a 3 T MAGNETOM Prisma system (Siemens Healthcare, Erlangen, Germany) using a Cartesian, fully sampled gradient echo FLASH (fast low angle shot) sequence and a flip angle of 10°. The images are reconstructed with the SOS combination technique as specified in Eqs. (2) and (6). The most important acquisition parameters are given in Table 3. The values of these parameters are adjusted to produce a target SNR of at least 8, which is necessary for the approximation in Eq. (10) to be within 1 % of the true value.

The flow velocity is encoded along the direction of the pipe axis with a sensitivity of $V_{enc} = 0.5$ m/s using the two-point measurement scheme. The water in all test cases is at room temperature (21°) and contains a concentration of 1 g/L Copper sulfate as contrast agent. Each test case is measured in a batch process consisting of 100 repeated MRV acquisitions. During this process, the experimental conditions are kept constant.

4.1 Noise distribution in the image

Figure 2 shows the image magnitude, the phase difference, and the standard deviation of the noise for all five test cases. The standard deviation of the noise is obtained from the multiple replica method in Eq. (27). The images are manually segmented into an artifact-free background (BG) and a ROI which contains the water. The results for test case 1 show that the image is free of motion artifacts. The

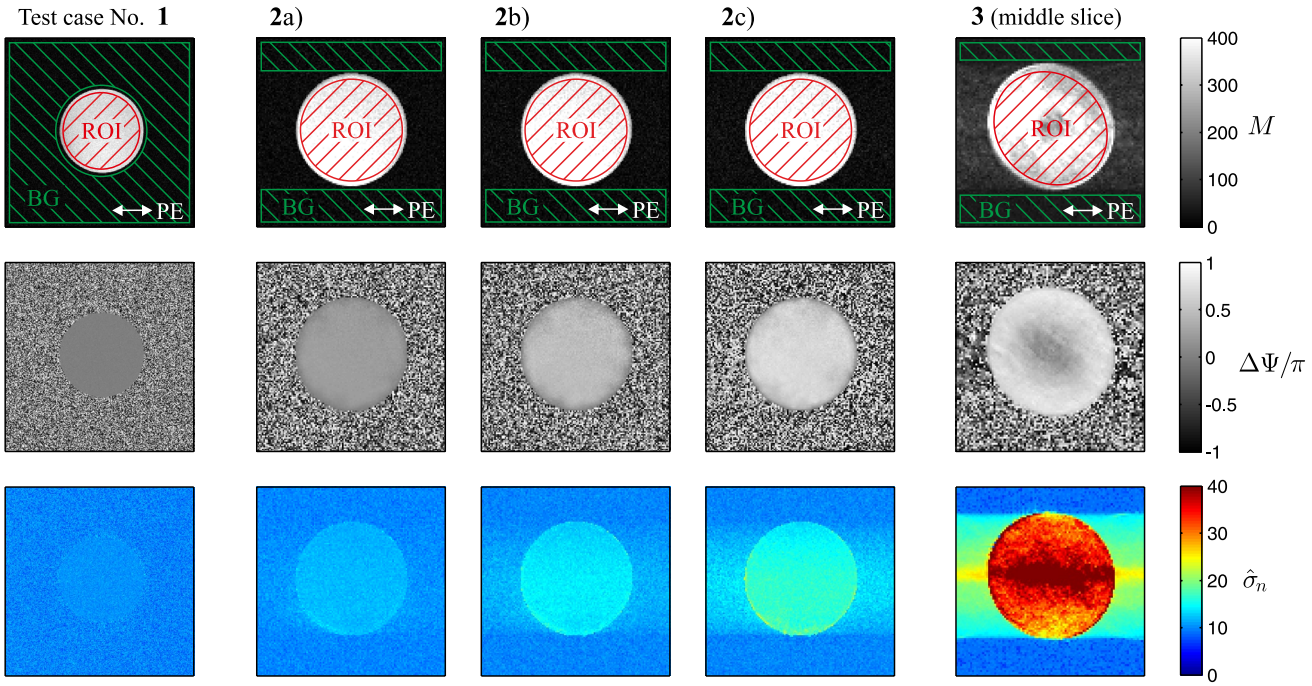

Fig. 2 Measurement results for all test cases. The *top row* and *center row* show the magnitude and phase difference of an individual image replica, respectively. The *bottom row* shows the standard deviation of the noise from Eq. (27). The image magnitude is scaled so that the standard deviation of the noise yields 10 in the artifact-free background. This scaling is arbitrary and does not affect the outcome. All magnitude values are integers. The manually segmented ROI and BG are defined by *red* and *green color*, respectively. *PE* indicates the phase encoding direction. Note that in the images of test case 3, the shape of the pipe cross-sectional area is skewed due to a misregistration of the rotating fluid

standard deviation of the noise is approximately constant across the image. The results for test cases 2 and 3 show a different characteristic. The standard deviation of the noise is increased in the ROI and in the image regions left and right of the ROI, hence along the phase encoding direction. In addition, the images show strong motion artifacts along the phase encoding direction as clearly visible in the image magnitude of test case 3. These effects becomes more pronounced with increasing test case number. For test case 3, the average standard deviation of the noise in the ROI is approximately four times higher than the standard deviation in the artifact-free background.

The increased noise in the image is caused by random signal fluctuations that arise from the turbulent flow. The mechanism of the noise increase is demonstrated by a numerical simulation. The simulation is set up similar to the presented measurements, hence with a Cartesian, fully sampled k-space. Two cases are investigated. In the first case, the signal in the sample is subject to complex white Gaussian noise. Thus, each phase encoding line in the k-space corresponds to a slightly different signal. The simulation results in Fig. 3 show that in this case, the noise is homogeneously increased along the phase encoding direction. The second case describes a scenario in which the complex signal is only changed in between acquisitions. In

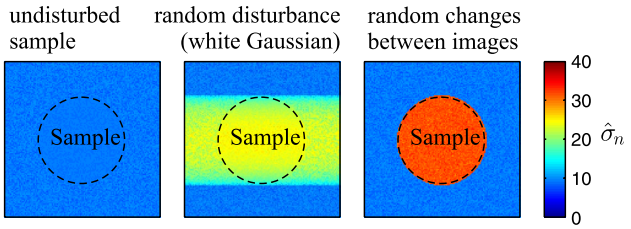

Fig. 3 Simulation of the noise distribution in images with Cartesian, fully sampled k-space and 128 × 128 voxels. The voxels in the sample are disturbed by a random fluctuation of the complex signal with standard deviation of 30. The background noise has a standard deviation of 10. The resulting standard deviation of the noise in the image is estimated with Eq. (27) based on 1000 simulated image replicas

this case, the noise increase is limited to the image region with the flow sample. In comparison with the measurement results in Fig. 2, it can be seen that both effects occur at the same time. The reason is that the turbulence in the flow is characterized by a broad range of time scales.

The specific effect in the image depends on the acquisition time and on the time scales in the flow. This can be explained as follows. With longer acquisition time and unchanged flow characteristics, a wider range of time scales contribute to signal changes between k-space lines.

The resultant effect will be a more homogeneous noise increase along the phase encoding direction. In the extreme case, in which the acquisition time is much longer than the longest time scale in the flow, the noise increase will be entirely homogeneous along the phase encoding direction, as in the middle image of Fig. 3. This is supposedly the case in conventional MRV measurements where the acquisition time lies in the order of minutes and longer.

4.2 Evaluation of the uncertainty estimators

The estimators from Sects. 3.1–3.4 are evaluated. The estimators based on manually segmented images ($\hat{\sigma}_{\mathrm{u,CA1}}$, $\hat{\sigma}_{\mathrm{u,ROI2}}$) use the same image regions as depicted in Fig. 2. The estimators based on a segmented histogram ($\hat{\sigma}_{\mathrm{u,CA2}}$, $\hat{\sigma}_{\mathrm{u,ROI1}}$) use a magnitude threshold to define these image regions. The segmentation of the histogram is demonstrated in Fig. 4. Using the data from test case 3, it is shown that the histogram of the image magnitude contains two clearly distinguishable parts. The left part of the histogram corresponds to the image background, and the right part corresponds to the ROI. The magnitude threshold is determined as the local minimum between these two histogram parts. The background part contains two peaks, one associated with the artifact-free background and a second, smaller peak associated with the motion artifacts along the phase encoding direction, as shown in Fig. 2. The two peaks overlap and as a result, it is not possible to isolate the artifact-free background by this segmentation technique. Similarly, not all data points in the ROI part belong to the actual flow sample. Some data points with weaker magnitude belong to voxels with partial volume effects at the edges of the flow volume. These voxels are excluded from the ROI in the manually segmented images.

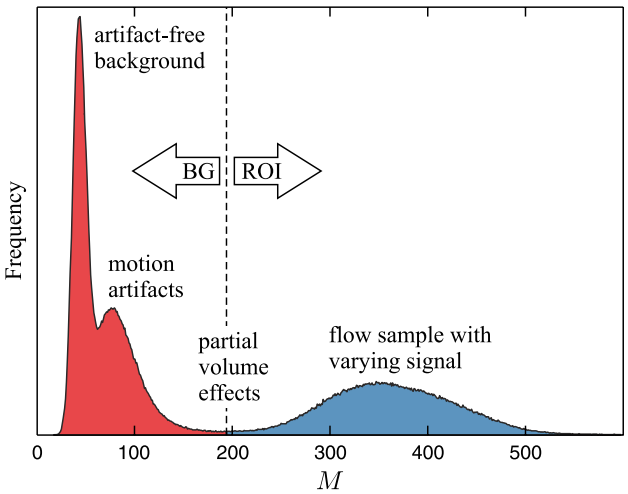

Fig. 4 Qualitative histogram of the magnitude data in the images of test case 3. The bin size is one. The magnitude threshold (*dashed line*) is determined as the local minimum between the two regions, BG and ROI

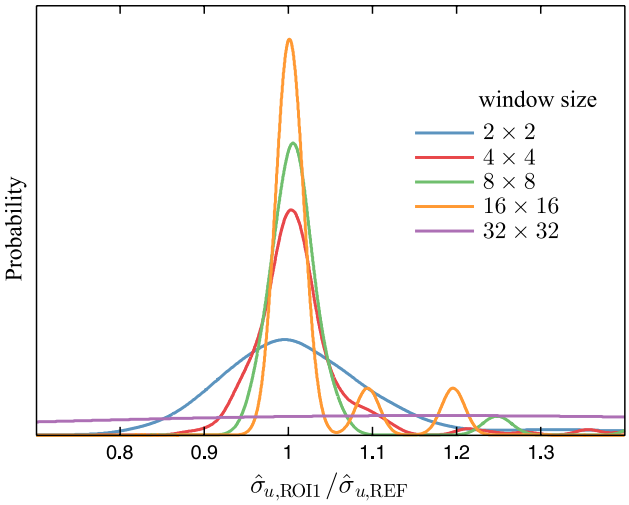

Fig. 5 Effect of the window size (measured in number of voxels) on the uncertainty estimator with local statistic from Sect. 3.3 ($\hat{\sigma}_{\mathrm{u,ROI1}}$). The depicted *curves* represent the distribution of the local estimates for test case 1 as obtained by the kernel density estimation

The local statistics approach used in Sect. 3.3 ($\hat{\sigma}_{\mathrm{u,ROI1}}$) requires a specification of the window size. The effect of different window sizes is demonstrated in Fig. 5. Using the data from test case 1, it is shown that the peak of the distribution of the local estimates is consistent for windows with up to 16×16 voxels. The issue that arises with smaller window sizes is that the distribution is wider and the peak of the distribution becomes less pronounced. As a compromise between accuracy and precision, a window size of 8×8 voxels was determined for test cases 1 and 2. The images of test case 3 contain stronger signal variations in the ROI and in this case, a window size of 6×6 voxels was found to yield the best result.

Using all available image replicas, the estimators based on individual images ($\hat{\sigma}_{\mathrm{u,CA1}}$, $\hat{\sigma}_{\mathrm{u,CA2}}$, $\hat{\sigma}_{\mathrm{u,ROI1}}$) are evaluated 100 times per test case. The estimator that uses image replica pairs ($\hat{\sigma}_{\mathrm{u,ROI2}}$) is evaluated 50 times per test case. Figure 6 shows the evaluation results. The black dots in the figure represent the mean of all estimates and the colored bars indicate the interval that contains 95 % of all estimates. It is shown that the two estimators based on the noise in the artifact-free background ($\hat{\sigma}_{\mathrm{u,CA1}}$, $\hat{\sigma}_{\mathrm{u,CA2}}$) become inaccurate for increasing test case number. These uncertainty estimators represent the conventional approach. The deviation is -75 % for test case 3. The estimator based on the noise in the ROI, hence the image region with flow, ($\hat{\sigma}_{\mathrm{u,ROI1}}$) is considerably more accurate for the same test cases. The same applies to the estimator that is directly based on the velocity deviations in the ROI ($\hat{\sigma}_{\mathrm{u,ROI2}}$). Note that all four

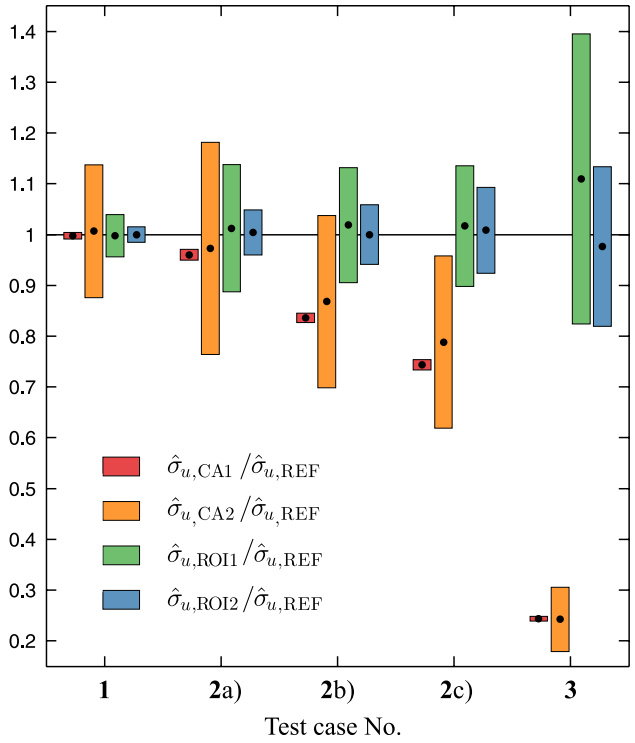

Fig. 6 Results of the uncertainty estimators from Sects. 3.1–3.4 compared to the reference values from Sect. 3.5. The *dots* represent the mean of all estimates and the *bars* indicate the interval that contains 95 % of all estimates

estimators produce accurate results for the images of test case 1 which contain homogeneous noise.

Finally, it is emphasized, that the precision of these estimators strongly depend on the number of voxels that contribute to the estimate. The images presented here contain less than 100,000 voxels, and much less in the segmented image regions. Actual MRV measurements can contain several 10,000,000 voxels. Accordingly, the precision of the estimators will improve significantly when applied to such data sets.

5 Discussion

The experiments suggest that the noise in the image is affected by the turbulent flow. The image is subject to motion artifacts and therefore to an increased noise in the phase encoding direction. The average standard deviation of the noise in the image region with flow was found up to four times higher than in the artifact-free background. This deviation translates directly to the estimation of the measurement uncertainty. It is therefore crucial whether the measurement uncertainty is based on the noise in the artifact-free background or on the noise in the image region with flow. The original guidelines for the estimation of the uncertainty in MRV do not make a reference on the different noise levels (e.g., Pelc et al. 1994). Consequently, the definition of the measurement uncertainty in MRV needs to be reconsidered. Two definitions are proposed:

1. *Background Uncertainty* This definition refers to the minimum achievable measurement uncertainty if the flow sample was perfectly stationary. The uncertainty can be estimated from the noise in the artifact-free image background which corresponds to the thermal noise from the MRI receiver chain and is unaffected by the turbulent flow. Possible uncertainty estimators are $\hat{\sigma}_{\mathrm{u,CA1}}$ and $\hat{\sigma}_{\mathrm{u,CA2}}$.
2. *Total Statistical Uncertainty* This definition corresponds to the standard deviation of the results if the experiment was repeated. The *Total Statistical Uncertainty* combines all statistical uncertainties and can be regarded as the actual measurement uncertainty of the experiment. As a possible approach, the uncertainty can be estimated from the noise in the image region with flow, which combines the thermal noise from the MRI receiver chain and the motion artifacts from the turbulent flow. Possible uncertainty estimators are $\hat{\sigma}_{\mathrm{u,ROI1}}$ and $\hat{\sigma}_{\mathrm{u,ROI2}}$.

An example to demonstrate the difference between these two uncertainty definitions is provided in Fig. 7. The figure shows a velocity measurement of test case 3. The depicted

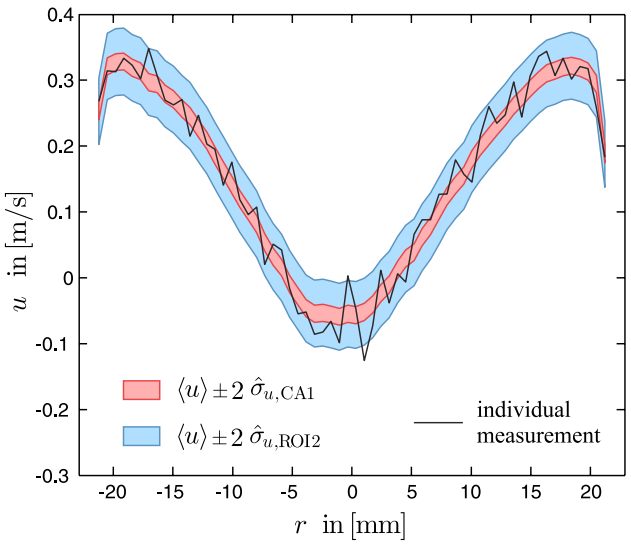

Fig. 7 Axial velocity distribution in the symmetry plane of test case 3. The velocity data from an individual measurement is compared to the expected value (the mean of all measurements, $\langle u \rangle$). The *colored areas* represent the 95 % confidence interval obtained from the two uncertainty definitions. The *Background Uncertainty* is evaluated with the estimator $\hat{\sigma}_{\mathrm{u,CA1}}$ from Sect. 3.1. The *Total Statistical Uncertainty* is evaluated with the estimator $\hat{\sigma}_{\mathrm{u,ROI2}}$ from Sect. 3.4

Table 4 Evaluation of the uncertainty definitions with previously published MRV data

Description of experiment	$\frac{\hat{\sigma}_{u,CA1}}{\hat{\sigma}_{u,ROI2}}$
Intake flow of an internal combustion engine model (Freudenhammer et al. 2014). Sudden flow expansion ($Re = 45{,}000$ at inlet)	0.34
Coaxial heat exchanger similar to Buchenberg et al. (2015). Low turbulence pipe flow ($Re = 1800$) with buoyancy driven cross-flow	0.63
Turbine blade cooling duct model (Bruschewski et al. 2016). Various geometries. Strongly swirling turbulent pipe flow ($Re = 20{,}000$)	0.27–0.56

The *Background Uncertainty* is evaluated with the estimator $\hat{\sigma}_{u,CA1}$ from Sect. 3.1. The *Total Statistical Uncertainty* is evaluated with the estimator $\hat{\sigma}_{u,ROI2}$ from Sect. 3.4

uncertainty intervals correspond to the double standard deviation (95 % confidence) which means that the measured velocity values should lie almost completely within these intervals. This is clearly not the case with the *Background Uncertainty*. The associated uncertainty interval does not represent the statistical variations of the velocity data. Obviously, the *Total Statistical Uncertainty* is a much closer representation of this measurement.

Generally, in images with low background noise and large degree of motion artifacts, the error of the *Background Uncertainty* will be most pronounced. In this study, the *Background Uncertainty* was found up to −75 % smaller than the *Total Statistical Uncertainty*. This observation is based on generic experiments with relatively small image size and in which the turbulence in the flow was produced on purpose. The question rises whether the same effect can be observed in actual MRV experiments. For this reason, the two uncertainty definitions are evaluated with the measurement data from previously published studies. The results are given in Table 4. It is shown that the difference lies in the same order of magnitude as observed with the experiments in this study.

Consequently, the conventional approach of estimating the uncertainty from the noise in the artifact-free background, hence the definition of the *Background Uncertainty*, is inaccurate. For future MRV experiments, it is therefore strongly recommended that the *Total Statistical Uncertainty* is evaluated instead. In the case that two or more image replicas are available, the uncertainty can be conveniently estimated with the dual acquisition estimator from Sect. 3.4. In experiments where only one image is available, the local statistics estimator from Sect. 3.3 can be applied.

In addition to the presented estimators, there are other methods conceivable. For example, the *Total Statistical Uncertainty* could be estimated in the background region which is affected by motion artifacts. However, this requires that the motion induced noise is homogeneous in the phase encoding direction, as for example in the middle image in Fig. 3. This method could not be tested here since the relatively short acquisition time of the measurements led to an inhomogeneous noise increase. The influence of the acquisition time on the homogeneity of the noise increase was explained at the end of Sect. 4.1.

Finally, it is emphasized that the difference between the *Background Uncertainty* and the *Total Statistical Uncertainty* also depends on the imaging technique. All presented measurements were obtained by conventional Cartesian sampling. In medicine, the issue of motion artifacts is often addressed with different imaging techniques that are less prone to motion. For example, radial schemes rotate the phase encoding direction to reduce motion artifacts (Zhang et al. 2010). With single shot echo planar imaging (EPI), motion artifacts are effectively removed (Poustchi-Amin et al. 2001). On the downside, these imaging techniques have other imperfections, for example they are more prone to a variety of other artifacts compared to conventional Cartesian sampling.

Consequently, with certain imaging setups, it might be possible to use the noise in the image background to calculate the *Total Statistical Uncertainty*. Nevertheless, the most reliable approach which is independent of the imaging setup, is to measure the uncertainty directly in the image region where the flow is measured, for example with the estimators from Sects. 3.3 and 3.4.

6 Conclusion

Over the past decade, velocity measurements with MRV have found increasing application in the field of engineering and science. An important research area that has been left out so far, is the estimation of the measurement uncertainty. This was the purpose of this study. Based on various test cases, it was found that the uncertainty estimate can vary substantially depending on how the uncertainty is obtained. The widely used approach of estimating the uncertainty from the noise in the artifact-free background can lead to a clear underestimation of the uncertainty value. These outcomes were also verified with the MRV data from other studies. Therefore, it is strongly recommended that the uncertainty estimate is obtained from the noise in the image region with the flow sample or that it is measured directly from the velocity data. Two uncertainty estimators

were presented which, depending on the specific requirements, can be applied in a straightforward manner.

Acknowledgments This work was supported by the Bundesministerium für Wirtschaft und Technologie (BMWi) under Grant Number 20T1108C.

References

Aja-Fernández S, Alberola-López C, Westin CF (2008) Noise and signal estimation in magnitude MRI and Rician distributed images: a LMMSE approach. Image Process IEEE Trans 17(8):1383–1398. doi:10.1109/TIP.2008.925382

Aja-Fernández S, Tristán-Vega A, Alberola-López C (2009) Noise estimation in single-and multiple-coil magnetic resonance data based on statistical models. Magn Reson Imaging 27(10):1397–1409. doi:10.1016/j.mri.2009.05.025

Benson MJ, Elkins CJ, Yapa SD, Ling JB, Eaton JK (2012) Effects of varying reynolds number, blowing ratio, and internal geometry on trailing edge cutback film cooling. Exp Fluids 52(6):1415–1430. doi:10.1007/s00348-012-1260-1

Bernstein MA, Grgic M, Brosnan TJ, Pelc NJ (1994) Reconstructions of phase contrast, phased array multicoil data. Magn Reson Med 32(3):330–334. doi:10.1002/mrm.1910320308

Bruschewski M, Scherhag C, Schiffer HP, Grundmann S (2016) Influence of channel geometry and flow variables on cyclone cooling of turbine blades. J Turbomach 138(6). doi:10.1115/1.4032363

Buchenberg WB, Wassermann F, Grundmann S, Jung B, Simpson R (2015) Acquisition of 3D temperature distributions in fluid flow using proton resonance frequency thermometry. Magn Reson Med. doi:10.1002/mrm.25874

Coletti F, Elkins CJ, Eaton JK (2013) An inclined jet in crossflow under the effect of streamwise pressure gradients. Exp Fluids 54(9):1589. doi:10.1007/s00348-013-1589-0

Constantinides CD, Atalar E, McVeigh ER (1997) Signal-to-noise measurements in magnitude images from NMR phased arrays. Magn Reson Med 38(5):852–857. doi:10.1002/mrm.1910380524

den Dekker AJ, Sijbers J (2014) Data distributions in magnetic resonance images: a review. Phys Med 30(7):725–741. doi:10.1016/j.ejmp.2014.05.002

Dietrich O, Raya JG, Reeder SB, Reiser MF, Schoenberg SO (2007) Measurement of signal-to-noise ratios in MR images: influence of multichannel coils, parallel imaging, and reconstruction filters. J Magn Reson Imaging 26(2):375–385. doi:10.1002/jmri.20969

Elkins CJ, Alley MT (2007) Magnetic resonance velocimetry: applications of magnetic resonance imaging in the measurement of fluid motion. Exp Fluids 43(6):823–858. doi:10.1007/s00348-007-0383-2

Freudenhammer D, Baum E, Peterson B, Böhm B, Jung B, Grundmann S (2014) Volumetric intake flow measurements of an IC engine using magnetic resonance velocimetry. Exp Fluids 55(5):1724. doi:10.1007/s00348-014-1724-6

Fukushima E (1999) Nuclear magnetic resonance as a tool to study flow. Annu Rev Fluid Mech 31(1):95–123. doi:10.1146/annurev.fluid.31.1.95

Gladden LF, Sederman AJ (2013) Recent advances in flow MRI. J Magn Reson 229:9–11. doi:10.1016/j.jmr.2012.11.022 (frontiers of in vivo and materials MRI research)

Griswold MA, Jakob PM, Heidemann RM, Nittka M, Jellus V, Wang J, Kiefer B, Haase A (2002) Generalized autocalibrating partially parallel acquisitions (GRAPPA). Magn Reson Med 47(6):1202–1210. doi:10.1002/mrm.10171

Grundmann S, Sayles E, Elkins CJ, Eaton J (2012a) Sensitivity of an asymmetric 3d diffuser to vortex-generator induced inlet condition perturbations. Exp Fluids 52(1):11–21. doi:10.1007/s00348-011-1205-0

Grundmann S, Wassermann F, Lorenz R, Jung B, Tropea C (2012) Experimental investigation of helical structures in swirling flows. Int J Heat Fluid Flow 37:51–63. doi:10.1016/j.ijheatfluidflow.2012.05.003

Gudbjartsson H, Patz S (1995) The Rician distribution of noisy MRI data. Magn Reson Med 34(6):910–914. doi:10.1002/mrm.1910340618

Hansen MS, Kellman P (2015) Image reconstruction: an overview for clinicians. J Magn Reson Imaging 41(3):573–585. doi:10.1002/jmri.24687

Henkelman RM (1985) Measurement of signal intensities in the presence of noise in mr images. Med Phys 12(2):232–233. doi:10.1118/1.595711

Issakhanian E, Elkins C, Eaton J (2012) In-hole and mainflow velocity measurements of low-momentum jets in crossflow emanating from short holes. Exp Fluids 53(6):1765–1778. doi:10.1007/s00348-012-1397-y

Kaufman L, Kramer DM, Crooks LE, Ortendahl DA (1989) Measuring signal-to-noise ratios in MR imaging. Radiology 173(1):265–267. doi:10.1148/radiology.173.1.2781018

Koay CG, Basser PJ (2006) Analytically exact correction scheme for signal extraction from noisy magnitude MR signals. J Magn Reson 179(2):317–322. doi:10.1016/j.jmr.2006.01.016

Lathi BP (1998) Modern digital and analog communication systems, 3rd edn. Oxford University Press, New York

Lo KP, Elkins CJ, Eaton JK (2012) Separation control in a conical diffuser with an annular inlet: center body wake separation. Exp Fluids 53(5):1317–1326. doi:10.1007/s00348-012-1360-y

Markl M, Frydrychowicz A, Kozerke S, Hope M, Wieben O (2012) 4D flow MRI. J Magn Reson Imaging 36(5):1015–1036. doi:10.1002/jmri.23632

Moran PR (1982) A flow velocity zeugmatographic interlace for NMR imaging in humans. Magn Reson Imaging 1(4):197–203. doi:10.1016/0730-725X(82)90170-9

NEMA (2014) Determination of signal-to-noise ratio (SNR) in diagnostic magnetic resonance imaging. NEMA Standards Publication MS 1-2008 (R2014). http://www.nema.org/Standards/Pages/Determination-of-Signal-to-Noise-Ratio-in-Diagnostic-Magnetic-Resonance-Imaging.aspx

Onstad A, Elkins C, Medina F, Wicker R, Eaton J (2011) Full-field measurements of flow through a scaled metal foam replica. Exp Fluids 50(6):1571–1585. doi:10.1007/s00348-010-1008-8

Pelc NJ, Bernstein MA, Shimakawa A, Glover GH (1991) Encoding strategies for three-direction phase-contrast MR imaging of flow. J Magn Reson Imaging 1(4):405–413. doi:10.1002/jmri.1880010404

Pelc N, Sommer F, Li K, Brosnan T, Herfkens R, Enzmann D (1994) Quantitative magnetic resonance flow imaging. Magn Reson Q 10(3):125–147. http://www.ncbi.nlm.nih.gov/pubmed/7811608

Piro M, Wassermann F, Grundmann S, Leitch B, Tropea C (2016) Progress in on-going experimental and computational fluid dynamic investigations within a CANDU fuel channel. Nucl Eng Design 299:184–200. doi:10.1016/j.nucengdes.2015.07.009

Poustchi-Amin M, Mirowitz SA, Brown JJ, McKinstry RC, Li T (2001) Principles and applications of echo-planar imaging: a review for the general radiologist 1. Radiographics 21(3):767–779. doi:10.1148/radiographics.21.3.g01ma23767

Pruessmann KP, Weiger M, Scheidegger MB, Boesiger P et al (1999) SENSE: sensitivity encoding for fast MRI. Magn Reson Med 42(5):952–962. doi:10.1002/(SICI)1522-2594(199911)42:5<952:AID-MRM16>3.0.CO;2-S

Reeder SB, Wintersperger BJ, Dietrich O, Lanz T, Greiser A, Reiser MF, Glazer GM, Schoenberg SO (2005) Practical approaches to the evaluation of signal-to-noise ratio performance with parallel imaging: application with cardiac imaging and a 32-channel cardiac coil. Magn Reson Med 54(3):748–754. doi:10.1002/mrm.20636

Roemer PB, Edelstein WA, Hayes CE, Souza SP, Mueller O (1990) The NMR phased array. Magn Reson Med 16(2):192–225. doi:10.1002/mrm.1910160203

Scott DW (2012) Multivariate density estimation and visualization. In: Handbook of computational statistics, Springer, pp 549–569. doi:10.1002/9781118575574.ch6

Sijbers J, Poot D, den Dekker AJ, Pintjens W (2007) Automatic estimation of the noise variance from the histogram of a magnetic resonance image. Phys Med Biol 52(5):1335. doi:10.1088/0031-9155/52/5/009

Sijbers J, den Dekker AJ (2004) Maximum likelihood estimation of signal amplitude and noise variance from MR data. Magn Reson Med 51(3):586–594. doi:10.1002/mrm.10728

Wassermann F, Hecker D, Jung B, Markl M, Seifert A, Grundmann S (2013) Phase-locked 3D3C-MRV measurements in a bistable fluidic oscillator. Exp Fluids 54(3):1487. doi:10.1007/s00348-013-1487-5

Zhang S, Block KT, Frahm J (2010) Magnetic resonance imaging in real time: advances using radial flash. J Magn Reson Imaging 31(1):101–109. doi:10.1002/jmri.21987